Two-photon printing of monolithic glass electrospray emitters with TPMS micro-architectures

Journal of Micromechanics and Microengineering

OPEN ACCESS

RECEIVED
17 March 2026

REVISED
1 June 2026

ACCEPTED FOR PUBLICATION
17 June 2026

PUBLISHED
10 July 2026

PAPER

Two-photon printing of monolithic glass electrospray emitters with TPMS micro-architectures

Bryce Kingsley[1,*], **Nikolaos Chalmpes**[2], **Stefan Bell**[1], **Zach Ulibarri**[1], **Emmanuel Giannelis**[2], **Sadaf Sobhani**[1] and **Elaine Petro**[1]

[1] Mechanical and Aerospace Engineering, Cornell University, Ithaca, NY, United States of America
[2] Materials Science and Engineering, Cornell University, Ithaca, NY, United States of America
[*] Author to whom any correspondence should be addressed.

E-mail: bjk234@cornell.edu

Keywords: electric propulsion, electrospray emitter, additive manufacturing, two-photon polymerization

Abstract

The performance of electrospray thrusters is limited by the precision and constraints of traditional emitter fabrication techniques, which often lack resolution, geometric flexibility, or material compatibility for optimal emitter design and fabrication. Here, we demonstrate a high-resolution additive manufacturing approach for fabricating monolithic fused-silica electrospray emitters using two-photon polymerization printing followed by thermal conversion. Triply-periodic-minimal-surface (TPMS) microporous structures were embedded within the emitter body to provide passive capillary transport of propellant to the emitter tip. Optical profilometry and electron microscopy confirm high geometric fidelity to the target design and uniform shrinkage of approximately 40% during thermal processing, with preservation of the TPMS architecture. Electrospray emission testing was performed with ionic liquid EMI-BF_4 propellant, demonstrating consistent emission across sequential voltage sweeps with onset voltages of 2.4–2.6 kV, linear current–voltage characteristics, and estimated single emitter thrust of 64 nN at specific impulse values exceeding 3000 s.

1. Introduction

Electrospray propulsion has emerged as a promising technology for small spacecraft, offering high efficiency, scalability, and precise thrust control in a compact form. Unlike traditional electric propulsion systems, such as Hall-effect or ion thrusters, electrospray thrusters operate at lower power levels, produce minimal plume divergence, and can achieve exceptionally high specific impulses. These characteristics make them especially attractive for CubeSats and other resource-constrained platforms that demand both propulsive flexibility and stringent mass and volume budgets.

The performance of electrospray thruster systems is strongly governed by the design and fabrication of the emitters, as these components directly influence the efficiency of the charged droplet and ion emission required to generate thrust. Historially, electrospray emitters have been fabricated using subtractive manufacturing techniques, with chemical and electrochemical etching (or electrochemical micromachining) [1–4], and plasma and reactive-ion etching [5–11] being among the most dominant emitter fabrication techniques used to-date. While these etching techniques are well-established and characterized across many industries, they present several disadvantages and challenges for electrospray emitter fabrication. Achieving the desired emitter geometry often requires multiple photolithographic masking and etching steps, and issues with nonuniform etching can lead to inconsistencies and defects in the fabricated emitters. Additionally, these processes typically lack the capability to control the internal geometry of the emitters, which can be crucial for efficient fluid transport to the emitter tip. Alternative subtractive fabrication techniques have been explored to address some of these challenges, such as the laser ablation method by Li *et al* [12] and the work of Natisin *et al* [13] using conventional CNC milling to

create borosilicate glass emitters. Despite the maturity of subtractive fabrication techniques for electrospray emitters, these processes remain fundamentally limited in their ability to independently control both the external and internal emitter geometry/structure. In particular, conventional methods do not readily enable integrated porous networks for capillary-driven transport to the emission site. This limitation is significant, as the internal structure of the emitter governs the wetting behavior and flow stability, which ultimately impacts electrospray performance. As a result, there remains a clear unmet need for fabrication approaches that provide complete control over emitter geometry, with engineered internal structures to support reliable and efficient propellant transport.

In recent years, additive manufacturing (AM) has emerged as a promising alternative for electrospray emitter fabrication [14–18]. These AM technologies offer key advantages over traditional subtractive techniques, including greater design freedom and broader design space, faster prototyping and development, and the ability to create highly complex three-dimensional structures that are extremely challenging or impossible with conventional manufacturing processes. By leveraging layer-by-layer construction, AM techniques provide discrete control over both the external and internal emitter structures, enabling the integration of tailored geometries that can enhance emitter performance and enable new architectures for electrospray thrusters. Among the broad range of AM technologies, two-photon polymerization (TPP) printing stands out as a particularly powerful technique for micro- and nanoscale fabrication, which is required for precise emitter fabrication [19–22]. TPP printing is a photolithographic printing process in which solid structures are formed from a photocurable resin via simultaneous two-photon absorption induced by a highly focused laser. The feature resolution of TPP printing is largely dependent on the focusing objective, enabling single-micron to sub-micron resolutions. Additionally, TPP printing supports a wide range of materials, including polymers [17, 21, 23], metals [24, 25], and ceramics [19, 26, 27].

In this study, we leveraged TPP printing to fabricate high-resolution electrospray emitters. The emitters were TPP-printed using a nanoparticle-free polymer organic-inorganic photocurable resin [28] which undergoes a chemical transformation into fused silica following moderate thermal treatment. Triply-periodic-minimal-surface (TPMS) microstructures are embedded within the printed emitters to provide integrated fluid transport. The embedded TPMS structures provide a network of interconnected micropores with a high surface-to-volume ratio, making them effective for distributing propellant to the emission site while maintaining structural rigidity. We evaluated the reliability and repeatability of TPP printing for emitter fabrication, characterizing geometric variations and tolerances of the printed emitters, and the effects of thermal processing and shrinkage. Finally, we experimentally tested the printed emitters using a standard ionic liquid propellant to evaluate their electrospray performance and beam characteristics. To the best of the authors' knowledge, this work represents the first demonstration of TPP-printed electrospray emitters that are subsequently converted into monolithic fused-silica structures while retaining microscale fidelity. Unlike prior TPP-based electrospray emitters, which are typically limited to polymeric materials and simple internal structures (e.g. capillaries) [17, 18, 29, 30], the approach presented here enables deterministic integration of microporous TPMS structures within the emitter body to provide passive capillary propellant transport. This combination of micron-scale fabrication resolution, internal fluidic structure, and fused-silica material conversion enables a previously inaccessible design space for electrospray emitter architectures.

2. Materials and methods

2.1. Emitter fabrication

2.1.1. Resin synthesis

The emitters were printed using an organic-inorganic photocurable resin originally formulated by Bauer *et al* [28]. The resin contains a polyhedral oligomeric silsesquioxane (POSS) backbone that chemically transforms into a fused-silica structure after moderate thermal treatment. The materials for resin synthesis were purchased from commercial suppliers. Acrylic polyoctahedral silsesquioxane with the general formula $(RSiO_{1.5})_n$ with $R = C_6H_9O_2$ and $n = 8$, 10, 12 was purchased from Hybrid Plastics (USA). Trimethylolpropane ethoxylate triacrylate and 2-benzyl-2-(dimethylamino)-4'-morpholinobutyrophenone were both purchased from Sigma-Aldrich. All chemicals were used as received without further purification.

The resin was prepared using the following protocol. First, 90 wt% acrylic polyoctahedral silsesquioxane POSS monomer was mixed with 8 wt% trimethylolpropane ethoxylate triacrylate and stirred for approximately 2 hr to form a homogeneous blend. Subsequently, 2 wt% 2-benzyl-2-(dimethylamino)-4'-morpholinobutyrophenone, serving as the photoinitiator, was added under UV-protected conditions,

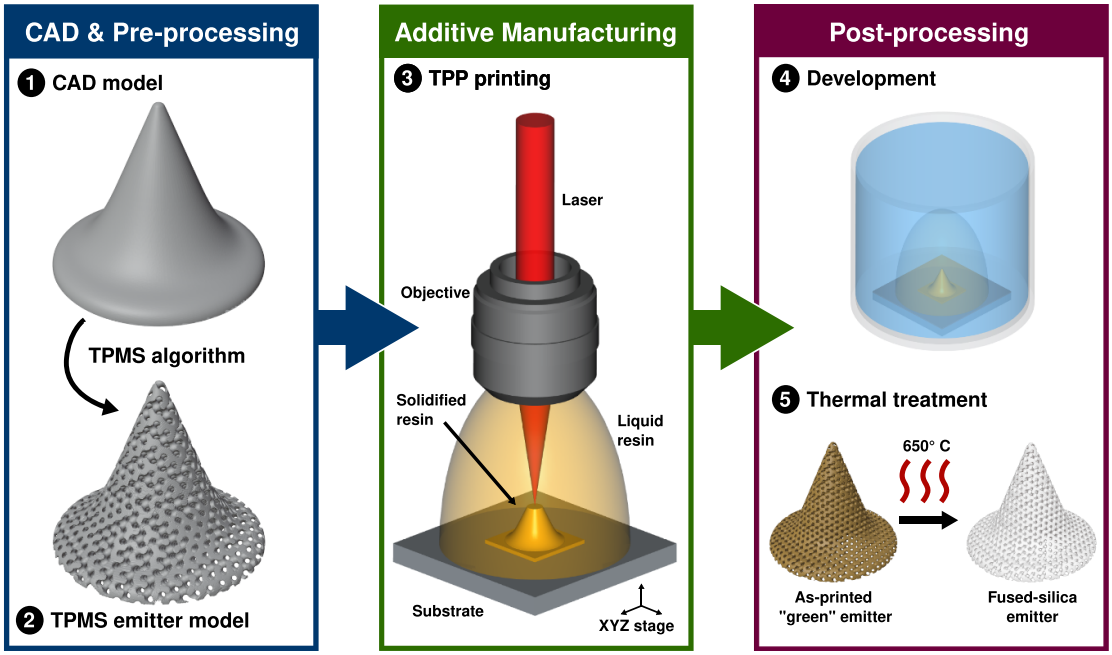

Figure 1. Overview of the emitter fabrication process.

and the mixture was stirred for 36 hr to ensure thorough dissolution. Finally, the solution was heated at 80 °C for 18 hr, which removed any residual photoinitiator particles and resulted in a transparent, uniform resin. After cooling to room temperature, the resulting resin was stable under ambient conditions and could be used for printing.

2.1.2. Emitter design and pre-processing

The emitter geometry was designed in two stages. First, the baseline geometry was modeled using standard computer-aided design (CAD) software (figure 1 step (1)). This baseline geometry served as a template in which the overall size and characteristic dimensions (tip radius, height, cone angle) were prescribed. Next, the template CAD model was processed using a geometric algorithm to embed TPMS lattice structure into the body of the emitter geometry, producing a porous internal structure as illustrated in step (2) of figure 1. The pore size and density of the TPMS structure can be tuned via input parameters of the geometric algorithm. For this work, the emitters were designed to the following target dimensions: 500 μm height, 20 μm tip radius, 25° cone half-angle, and 10 μm TPMS pore size.

2.1.3. TPP printing

In TPP printing, a near-infrared (NIR) laser is projected through a microscope objective and precisely focused within a volume of liquid photosensitive resin, as illustrated in step (3) of figure 1. The resin is specially formulated such that the activation wavelength (to initiate cross-linking) is half the baseline wavelength of the NIR laser beam, allowing most of the beam to pass through the resin with no interaction. Photon confinement near the beam's focal point induces simultaneous two-photon absorption, resulting in double the beam energy to reach the required activation wavelength/energy of the resin and initiate cross-linking, forming a solidified volume (voxel) surrounding the focal point. To enable 3D printing, the substrate is attached to precision linear stages, and the NIR laser is steered using a system of motorized galvo mirrors (not illustrated in figure 1). Analogous to other 3D printing techniques, the part is printed in a layer-by-layer manner by scanning the laser in the X–Y plane to define individual hatch (print) lines and incrementally stepping the stage in the Z direction to form successive layers.

The printing resolution of TPP is largely dependent on the pulse rate of the NIR laser and the magnification of the focusing objective. For this work, the emitters were printed using the commercially available Photonic Profession GT2 printer (Nanoscribe GmbH) equipped with a femtosecond laser and 10X microscope objective. The 10X objective was selected to maximize the printing field (approx. 1 mm) and minimize print time (lower magnification results in a larger voxel size, requiring less layers). To prepare for printing, the emitter CAD mesh was processed using the DeScribe slicing software provided by Nanoscribe. The TPP printing parameters used for fabricating the emitters are reported in table 1. Hatching distance was kept at the default value of 1 μm for the 10X objective on the GT2 printer.

Table 1. Two-photon printing parameters.

Parameter	Value
Laser power	120 mW (100% full power)
Microscope objective	10X
Voxel size ($W \times H$)	1.2 μm × 6 μm
Slicing distance (Z)	1 μm
Hatching distance (X–Y)	1 μm
Base scan speed	50 mm s^{-1}
Core scan speed	100 mm s^{-1}

Slicing distance was reduced to 1 μm (5 μm default) to best resolve the intricate TPMS structure. The first 3 layers were printed at half scan speed (50 mm s^{-1}) to improve adhesion to the substrate, and the rest of the structure was printed at full scan speed (100 mm s^{-1}) to minimize print time.

Silicon coupons were used as printing substrates due to their excellent surface uniformity and ease of use with the GT2 system. Prior to printing, the silicon substrates were cleaned via 5 min sonication in acetone, followed by 5 min sonication in isopropyl alcohol (IPA) to eliminate any potential residue from the acetone, and finally dried with compressed nitrogen. A small volume of POSS resin was dispensed via syringe onto a cleaned silicon substrate, and loaded into the GT2 printer. The print job (generated by DeScribe) was loaded into the NanoWrite software (Nanoscribe), and the emitter geometry was printed. After printing, the substrate (with the printed emitter geometry attached) was removed and developed in two sequential 10 min IPA baths (20 min total development) to dissolve and clear away unexposed POSS resin (figure 1 step (4)). Following development, the emitters were removed from the IPA bath and set aside to dry naturally before thermal treatment.

The print time for the emitters reported here was approx. 8 min per emitter, which is sufficiently fast enough for rapid prototyping and testing of single emitters. However, the total printing time can accumulate quickly when scaling to large emitter arrays (e.g. 13–14 h of continuous printing for a 10×10 array). These long array print times can be significantly reduced by minor adjustments to the printing parameters. In particular, increasing the slicing distance reduces the number of required layers and can greatly lower print time, at the expense of reduced printing resolution and fidelity. Although not reported here, we have found that emitters can be printed at 2 μm slicing distance with sufficient resolution but half the per-emitter print time (approx. 3–4 min), improving the scalability of this fabrication process to large arrays.

2.1.4. Thermal post-processing

Thermal post-processing was performed to convert the exposed POSS resin into fused silica, as illustrated in step (5) of figure 1. Here, we followed the three-stage thermal profile prescribed by Bauer *et al* [28], as follows: (1) constant linear ramp at 1 °C min^{-1}, (2) soak at 650 °C for 60 min, and (3) cool naturally to room temperature with the oven off. Thermal processing was conducted in air using a programmable muffle furnace (Nabertherm L3/11 240 V) for precise temperature control.

2.2. Emitter characterization

2.2.1. Geometric and structural analysis

The geometry and structure of the emitters was characterized using scanning electron microscopy (SEM) and 3D optical profilometry. The microstructure and resolution of the TPP-printed emitters was analyzed using a Zeiss Sigma 500 SEM, with accelerating potentials of 1–2 kV to mitigate charging effects on the insulative materials. 3D optical profilometry was performed using a Keyence VK-X260 confocal laser profilometer, equipped with the 10X microscope objective. Optical profilometry was used to evaluate the reliability/repeatability of TPP printing emitters, as well as the variability/tolerance between printed emitters and the target CAD emitter geometry.

2.2.2. Electrospray emission testing

The electrospray emission performance of the TPP-printed emitters was evaluated by experimental test-firing using standard ionic liquid propellant. To load an emitter for firing, 50 μl of 1-ethyl-3-methylimidazolium tetrafluoroborate (EMI-BF_4) was manually dispensed near the emitter base using a syringe. The emitter was left stationary for up to 2 min to allow the EMI-BF_4 to passively wick into the porous TPMS structure and fill the emitter to the tip (though, in many cases complete wicking occurred in under 30 s). Excess propellant on the silicon substrate near the base of the emitter was carefully removed using a tissue, with a small (unmeasurable) volume of propellent left near the emitter

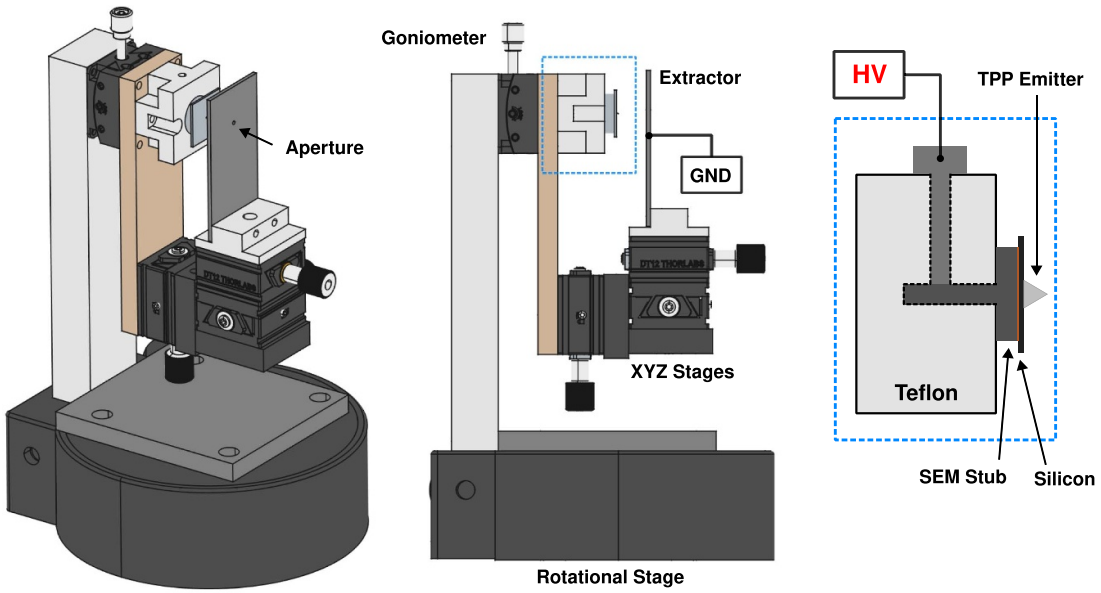

Figure 2. Schematic of the electrospray source used for characterizing TPP-printed glass emitters.

base to act as a reservoir. The retained volume in the porous emitter was not readily measurable, but can be estimated at approximately 10–20 nL based on the emitter geometry and porosity of the TPMS microstructure. The large volume of dispensed propellant (relative to the much smaller open volume of the emitter) was used to provide enough liquid to equally distribute it around the perimeter of the emitter base and promote uniform wetting. Propellant loading was performed under a microscope for visual confirmation of propellant wetting to the emitter tip.

The electrospray source used for testing is illustrated in figure 2. The silicon substrate with TPP-printed glass emitter was secured to a metal SEM stub using double-sided copper tape. The pin of the SEM stub was inserted into a machined teflon block and secured in place using a metal set screw. The high-voltage (HV) supply was attached to the set screw to supply the emission potential for electrospray. The extractor plate (0.5 mm thick, 1.5 mm aperture diameter) was attached to ground (GND) and mounted opposite the silicon substrate on a set of *XYZ* manual linear stages for alignment of the extractor aperture with the emitter. Emitter alignment was performed by eye and confirmed via optical microscope. The emitter-extractor distance (emitter tip to extractor) was positioned to approx. 500 μm. A goniometer was used to adjust the pitch of the emitter and extractor, and a horizontal rotation stage was used for adjusting the yaw. All emission testing and diagnostics were performed inside a vacuum chamber, with typical operating pressure of approx. 50–100 μTorr.

3. Results and discussion

3.1. Structure characterization

3.1.1. 3D optical profilometry and geometric variability

Precision and repeatability are key metrics in emitter fabrication, particular for large-scale or full-sized emitter arrays where geometric variations and inconsistencies between neighboring emitters can negatively impact beam uniformity and performance. To investigate the reliability and repeatability of TPP emitter fabrication, a collection of 10 emitters were printed using an identical design (same CAD model and print job). Each emitter was characterized with 3D optical profilometry before and after thermal treatment to evaluate geometric variability across the collection of emitters, and to identify any changes in geometry introduced during thermal processing.

Figures 3(a) and (b) shows 3D surface plots of a TPP-printed emitter before (a) and after (b) thermal processing, illustrating the pronounced reduction in emitter height and base diameter resulting from thermal shrinkage. This effect can be more clearly observed by the extracted 2D profiles plotted in figure 3(c). Each profile (green and red) contains 10 measurements (1 measurement for each of the 10 emitters analyzed), with the mean profile plotted as the solid lines and the shaded regions representing ± 1 standard deviation from the mean profile. The profile of the target emitter geometry was

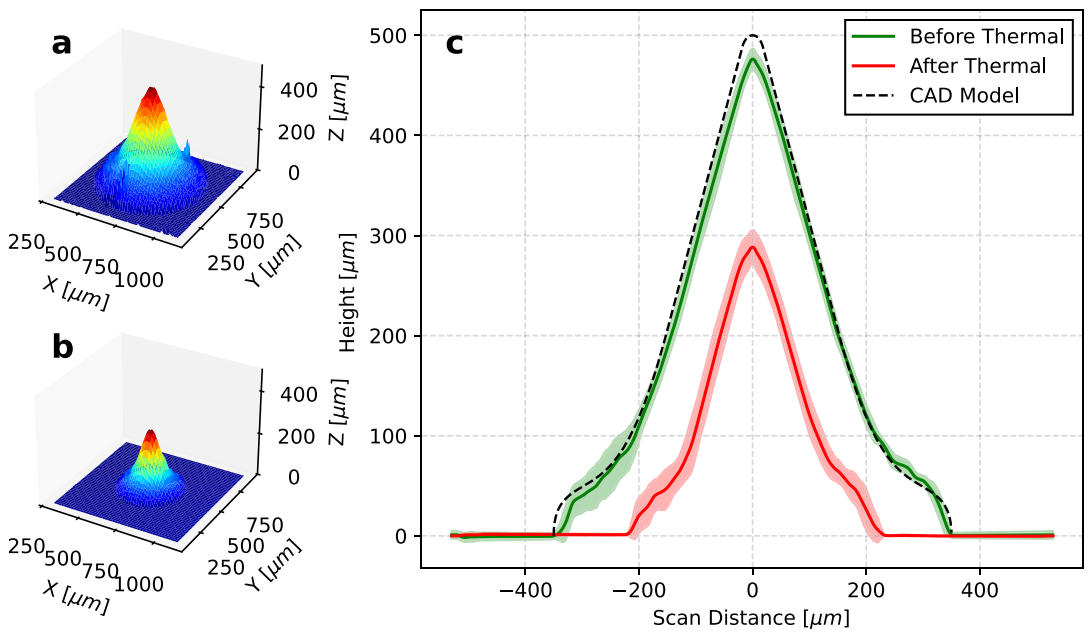

Figure 3. 3D optical profilometry scans of a printed emitter (a) before and (b) after thermal treatment, and (c) 2D scan profiles before (green) and after (red) thermal treatment. Solid colored lines show the mean profile, with shaded regions representing ± 1 std. Black dashed line shows the target CAD geometry.

extracted from the CAD model (prior to the TPMS algorithm) and is plotted as the dashed black line. All of the extracted emitter profiles were aligned in the axial (vertical) direction using the silicon substrate as the zero-point. Lateral (horizontal) alignment was performed by defining a vertical axis of symmetry for each profile which passes through the profile maximum (i.e. the emitter tip), and then aligning these symmetry axes at X = 0.

Prior to thermal treatment (green) all of the measured emitters exhibit minimal geometric variability and closely match the target CAD emitter profile. The greatest error between the measured profiles and CAD profile is observed near the tip (i.e. at $x = 0$), with a difference in height of approx. 20–25 μm to the target height (500 μm). The exact cause for this error is currently not known. However, we have observed that the TPP-printed structures shrink a small amount (<5% volumetric) during the drying stage following IPA development, which is suspected to have a negative effect on the printed emitter height. Profilometry measurements taken after thermal treatment (red) show significant shrinkage of the emitters in both axial (Y) and lateral (X) dimensions. The average emitter height dropped from approx. 480 μm to 280 μm due to thermal shrinkage, and the base diameter contracted from approx. 700 μm to 400 μm. This corresponds to approx. 42% axial and 38% lateral shrinkage, which are consistent with previously reported thermal shrinkage values for the POSS printing resin [28]. While the magnitude of shrinkage was significant, the shrinkage uniformity (i.e. axial and lateral shrinkage nearly the same) allowed the overall emitter shape/profile to be well-maintained following thermal treatment, effectively creating a scaled-down version of the pre-thermal and target CAD emitter geometries. Thermal treatment also introduced increased geometric variability between each measured emitter, indicated by the wider spread of the shaded red region particularly near the base of the emitters. However, the increased variation remains sufficiently low as to not greatly impact the repeatability and reliability of the emitter TPP printing process.

3.1.2. Microstructure validation

SEM was performed to evaluate the microstructure and resolution TPP-printed electrospray emitters. For SEM analysis, a TPMS microporous emitter was printed and SEM images were captured of the emitter before and after thermal treatment to investigate any effects of thermal shrinkage on microstructure.

Figure 4 presents SEM images of a TPP-printed microporous electrospray emitter before (left column) and after (right column) thermal processing. The top-most row (a) and (b) shows full-view images of the overall emitter geometry, and the zoomed-in views (c) and (e), and (d) and (f) focus on the detailed TPMS microstructure and surface texture. At the full-emitter scale ((a) and (b)) there are no observed changes/effects from thermal treatment on the emitter shape or TPMS microstructure. The

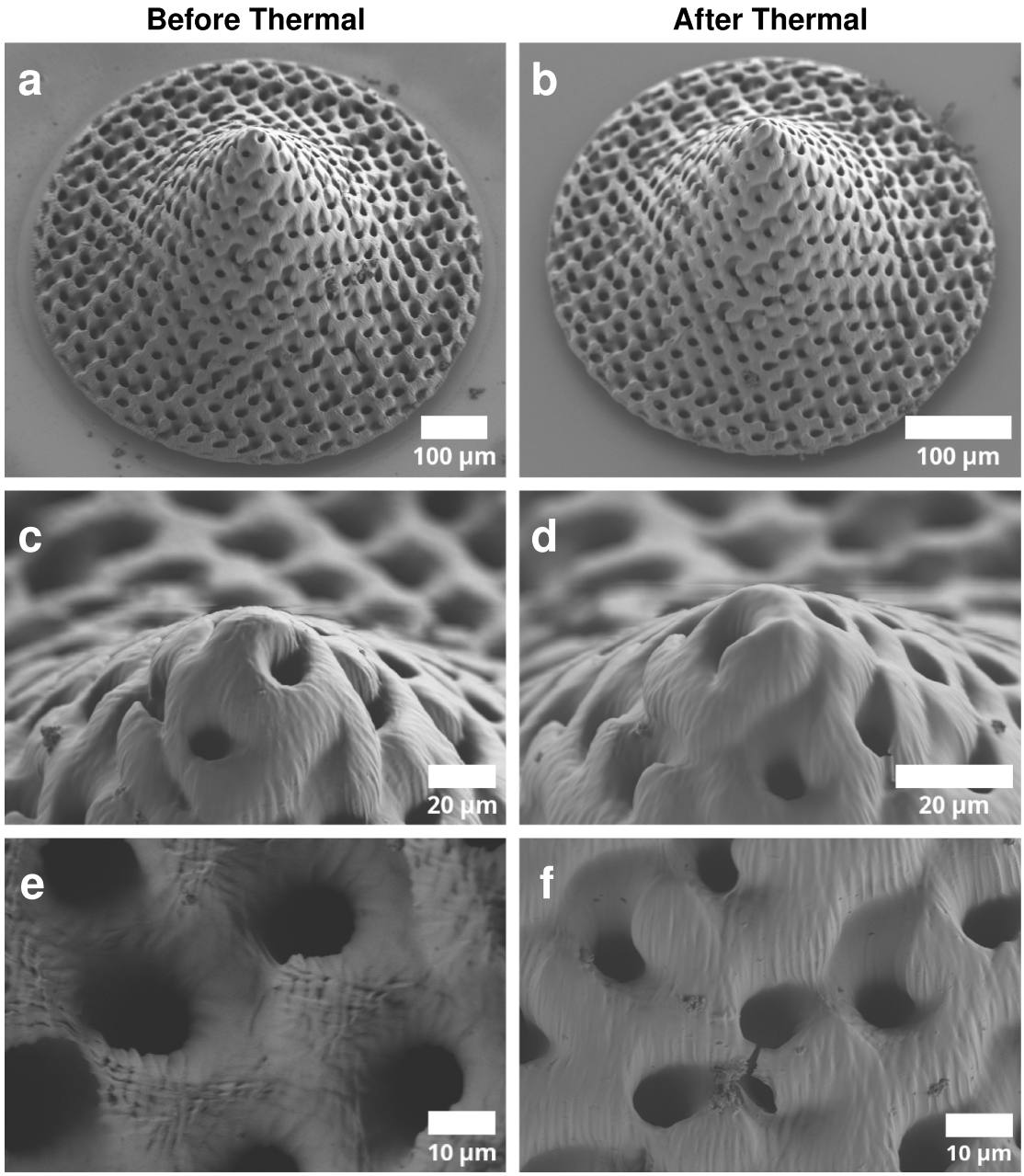

Figure 4. SEM images of a TPP-printed emitter before (left column) and after (right column) thermal processing. The emitter tip is shown in the middle row (c) and (d), and close-up images of the pores are presented in the bottom row (e) and (f).

overall emitter shape and TPMS structure look almost identical when comparing the pre-thermal and post-thermal images. In fact, the effects of thermal shrinkage is only visually evident in figure 4(a) and (b) by the difference in scale bars labeled on the respective images. These findings are consistent with the profilometry measurements of figures 3(c), highlighting the uniformity of thermal shrinkage which effectively scales-down the emitter geometry while maintaining (with high fidelity) the intricate TPMS microstructure.

Neglecting shrinkage, the full-scale SEM images (figures 4(a) and (b)) and profilometry measurements (figure 3(c)) show no significant effects on the overall emitter geometry and structure. However, the higher magnification images of figures 4(c)–(f) reveal some changes in surface roughness and TPMS pore morphology resulting from thermal treatment. Before thermal treatment (figures 4(d) and (f)) the pores exhibit irregular, jagged boundaries, with visible printing (hatch) lines and artifacts, and a rough surface texture. After thermal treatment (figures 4(d) and (f)) the surface appears significantly smoother and densified, which suggests localized material reflow and relaxation that occurs during the thermal treatment to convert the POSS resin into fused silica. Here, the effects of thermal shrinkage can be observed by comparing the TPMS pore diameter, which measures approx. 10–12 μm before thermal

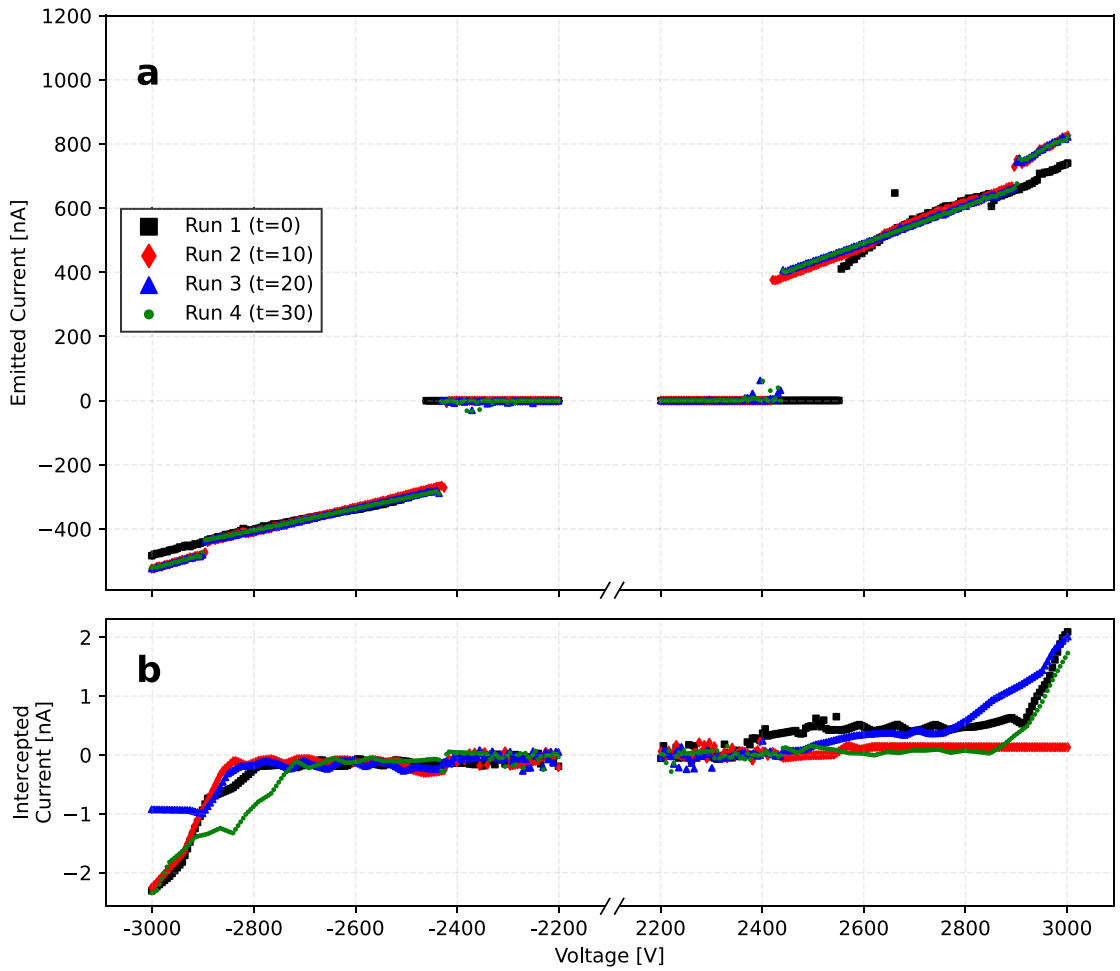

Figure 5. Emission characteristics of a TPMS porous glass electrospray emitter operating with EMI-BF_4 propellant. (a) *I–V* curves recorded over four consecutive runs at intervals of 10 min in both positive and negative polarities. (b) Corresponding intercepted current traces for each run.

treatment and 6–8 μm after thermal treatment. This equates to approx. 40% shrinkage in pore diameter which is consistent with the shrinkage results of in figure 3(c).

3.2. Electrospray emission performance

The emission characteristics of the TPP-printed electrospray emitters were evaluated using direct current–voltage (*I–V*) measurements. This diagnostic provides insight into key electrospray operating parameters, including onset voltage (to initiate emission) and emission linearity. To perform *I–V* measurements a HV source (Keithly 2567A SMU) was attached to the HV connection on the emitter block (figure 2), and the extractor was grounded through a picoammeter (Keithly 6485) to monitor for intercepted current on the extractor. Control software (Keithly Kickstart) was used to linearly ramp the applied voltage at a rate of ± 10 V s^{-1} until a maximum of ± 3 kV. To evaluate repeatability of firing, *I–V* measurements were captured over 4 consecutive runs, all performed under the same pump-down of the vacuum chamber. For each of the 4 runs, the voltage was first ramped in positive mode, followed by a reset to 0 V before initiating the negative ramp. Figure 5(a) plots the emission current (recorded from the source unit) vs. applied voltage of a TPP-printed emitter fired with EMI-BF_4 propellant. The colors of the datapoints represent consecutive runs, as denoted in the legend with the respective start timestamps $t = 0, 10, 20, 30$ (in minutes). The intercepted current on the extractor electrode is plotted in figure 5(b) for each run. In both plots (a) and (b) the region from -2200 V to 2200 V has been omitted for clarity, as no emission occurred within this voltage range.

The *I–V* curves of figure 5(a) show highly linear emission behavior in both positive and negative firing modes across all four runs, with emission currents reaching approx. 800 nA at $+3$ kV and -500 nA at -3 kV. However, closer inspection of the emission regime reveals a clear distinction in *I–V* trend of the initial run (Run 1) compared to the subsequent runs (Run 2–4). Run 1 has the highest onset voltage of approx. 2.55 kV, compared to 2.4–2.45 kV onset voltages of the following runs. Similar transient

emission behavior and *I–V* variability has been previously reported for passively-fed porous electrospray emitters [31–34]. These effects have been attributed to the coupled dynamics of fluid redistribution within the porous structure, stochastic activation of emission sites, and sensitivity of the emission process to the instantaneous filling state of the emitter. In particular, variations in fluid distribution and capillary-driven flow can lead to measurable changes in onset voltage and emission current during initial operation before a steady-state is established. Here, this initial conditioning process is reflected in Run 1, after which the emitter consistently exhibits a lower onset voltage and nearly identical *I–V* trends across Run 2–4, suggesting steady-state operation. An interesting characteristic can be observed in the *I–V* traces of figure 5(a) for Run 2–4, in which there is a sharp jump in emission current of approx. $\pm$50 nA at $\pm$ 2.9 kV. We suggest that this may result from the formation of secondary emission site(s) at exposed pores near the emitter tip, resulting in a net increase in emitted current.

Intercepted current on the extractor electrode is plotted in figure 5(b) over the same voltage range as the *I-V* curves, reaching a maximum of approx. $\pm$2 nA at the end of each voltage sweep ($\pm$3000 V), which equates to $<$ 1% total interception. With the exception of the positive sweep of Run 2 (red), the intercepted current remained fairly consistent across each run at $\leqslant$ 0.5 nA until approx. 2800 V , after which it increased with increasing voltage. This increase of intercepted current occurs near the observed jump in the *I-V* traces plotted in figure 5(a), and is likely the result of elevated space-charge effects and/or secondary emission sites which cause the electrospray plume to broaden, increasing interception on the extractor electrode.

The *I–V* traces presented in figure 5 were acquired during a single vacuum pump-down without propellant reloading between runs in order to evaluate short-term sweep-to-sweep repeatability during continuous operation. The measured onset voltage and current response remained consistent across sequential sweeps, indicating repeatable emission behavior over the duration of testing. The authors note that emission following propellant reloading was qualitatively assessed, and emission was achieved using fresh propellant. However, reload-to-reload reproducibility, onset-voltage reproducibility, and fixed-voltage stability were not systematically quantified in this study. More comprehensive repeatability and reproducibility testing is planned for future work to assess emitter performance and stability across multiple propellant loading cycles.

3.3. Beam characterization

3.3.1. Time-of-flight (TOF)

TOF mass spectrometry is a standard diagnostic for characterizing ion composition and charge-to-mass distribution in electrospray beams [35, 36]. The TOF system used in these analyses is described in greater detail by Hofheins *et al* [37]. Briefly, an electrostatic deflection gate is positioned between the electrospray source and the flight tube, with a microchannel plate (MCP) detector at the terminating end of the tube. The deflection gate is pulsed with a high voltage (2–3 kV) at a controlled frequency, allowing a narrow packet of ions to enter the flight tube. The ions traverse the flight tube, and their arrival times are captured at the MCP relative to the gate trigger. The resulting time (velocity) traces can be converted into mass spectra (due to velocity scaling with charge-to-mass ratio), revealing the composition and charge states of the electrospray products. Here, TOF measurements were taken both with the beam on-axis (i.e. source alignment with the flight tube), and with the beam slightly off-axis (approx. 5–10°), allowing characterization of spatial variations in beam composition.

Figure 6 plots the TOF characterization of the TPP-printed glass electrospray emitter fired with EMI-BF_4, in both positive (blue) and negative (red) firing modes. Spectra were acquired on-axis near the beam center (a) and off-axis (b) to probe spatial variations across the plume. For analysis, the acquired spectra were processed using a Savitzky-Golay filter (window size 11, polyorder 1) to smooth out the noise. Each trace in figure 6 is normalized and plotted versus mass-to-charge on a semi-logarithmic axis, with the expected masses of the monomer ($n = 0$), dimer ($n = 1$), and trimer ($n = 2$) species denoted by the vertical dashed lines. In both positive and negative operating modes the steps in the measured TOF current occur near the expected mass values of the monomer, dimer, and trimer species for EMI-BF_4. However, comparing the on-axis measurement (a) with the measurements taken slightly off-axis (b), we see a significant difference in the TOF signals. On-axis (near the beam center), there is a gradual non-linear increase/decrease in current across each step. Natisin *et al* reported a similar TOF current trend for their CNC-machined electrospray thrusters, suggesting that it results from increased species fragmentation in acceleration region of the beam causing a spread in the energy of the emitted ions [13]. In comparison, the TOF signals captured off-axis (figure 6(b)) show much more pronounced flat steps with minimal to no increase in current across steps, which is significant of well-defined monomer and dimer species, and minimal fragmentation. Additionally, the on-axis spectra (figure 6(a)) shows a modest high-mass tail in both positive and negative operating modes (i.e. non-zero current beyond 10^3

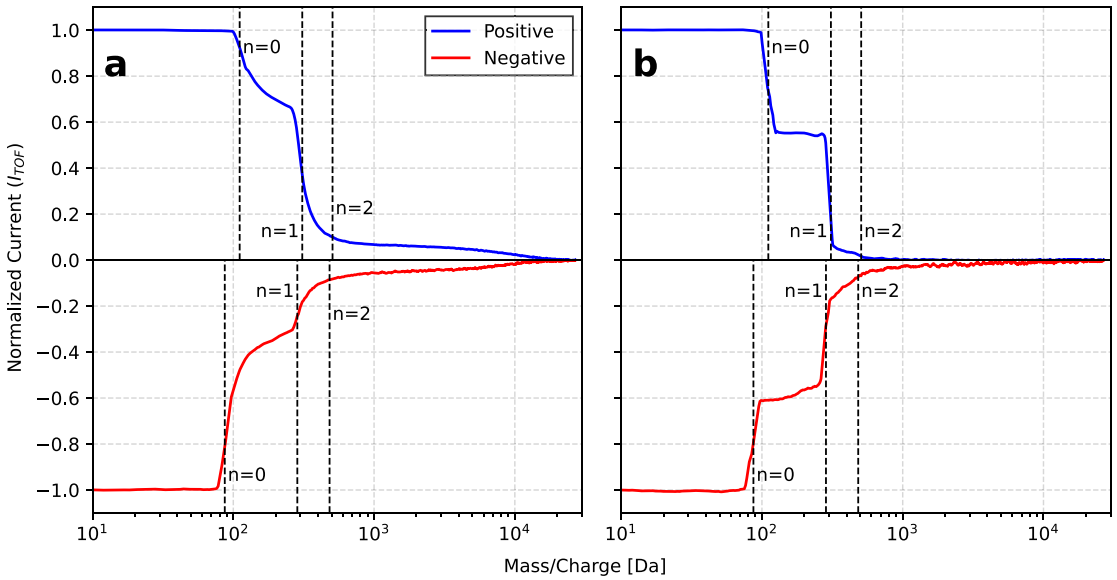

Figure 6. Time-of-flight (TOF) mass spectra collected from a TPP-printed glass electrospray emitter operating with EMI-BF_4 at ±2.5 kV. Plot (a) shows spectra recorded near the beam center, and (b) presents the spectra collected off-axis. Traces correspond to positive (blue) and negative (red) emission modes, as indicated in the legend. The distinct steps in the spectra correspond to different charge states ($n = 0, 1, 2$), with variations between on-axis and off-axis measurements highlighting differences in species distribution across the beam.

Table 2. Estimated beam composition from TOF measurements.

Spectra	% Monomer ($n = 0$)	% Dimer ($n = 1$)	% Trimer/Heaver species/Droplets ($n \geqslant 2$)
On-axis	30 (60)	55 (30)	15 (10)
Off-axis	45 (40)	50 (50)	5 (10)

Da), in contrast to the off-axis measurements which show little to no detected high-mass species. These findings reveal a spatially-variable beam composition, with the outer region of the beam predominantly composed of lower-mass monomer and dimer species, in contrast to the center of the beam which contains a greater quantity of fragmentation products and droplets/higher-mass species. This spatial variation in species distribution is consistent with known mechanisms governing angular dispersion in electrosprays. One contributing factor is charge-to-mass-dependent acceleration, wherein species with higher charge-to-mass ratios (e.g. monomers and dimers) experience greater electrostatic acceleration, resulting in higher velocities and increased angular divergence, while heavier species and droplets remain more confined near the beam axis due to their lower charge-to-mass ratios and greater inertia. However, the on-axis distribution of heavier species may also reflect a more complex, non-uniform beam structure. In particular, recent studies have suggested the presence of a more collimated, cone-jet-like core region within the electrospray plume of predominantly droplets and higher-mass species, surrounded by a ring of smaller ions [38–40]. 2D angularly-resolved TOF measurements have revealed the beam structure across many electrosprays is non-uniform and is currently an active area of research to explain why.

The composition of the electrospray beam can be estimated using the current amplitude from the TOF traces of figure 6. Estimates of beam composition from TOF spectra are presented in table 2. The values inside and outside the parenthesis represent negative and positive emission modes, respectively.

3.3.2. Beam angular measurements

Angular current measurements were captured to evaluate the alignment and divergence of the beam emitted by a TPP-printed emitter. These measurements were performed by adjusting the pitch (Y-angle) and yaw (X-angle) of the electrospray emitter using the goniometer and rotational stage (figure 2), and measuring the downstream current as a function of angular position. The angular mapping system used for these analysis is described in detail by Ulibarri *et al* [39, 41]. Briefly, the goniometer and rotational stage are attached to remotely-controlled stepper motor system for automated position and 2D angular mapping. To measure the beam current, a small electrode was placed downstream (approx. 60 mm from the extractor) and connected to a pico-ammeter for monitoring and recording the current reaching the

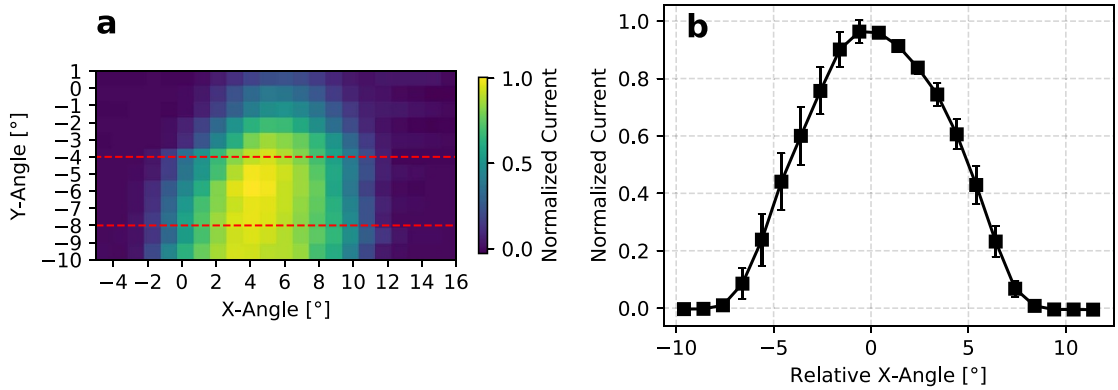

Figure 7. (a) 2D current heatmap showing beam intensity as a function of angle of the electrospray emitter in both the yaw (X) and pitch (Y) angles. Brighter regions correspond to higher measured current densities, as denoted in the colorbar. (b) 1D profile of average current as a function of centered yaw angle (beam centered at 0°), with error bars representing ±1 std.

electrode. This diagnostic technique creates an angularly-resolved 2D view of the beam shape, providing identification of the beam center and beam divergence/spread, and captures transient evolution of the beam structure.

Figure 7(a) shows a 2D heatmap of average detected current as a function of yaw and pitch angles. The downstream current was recorded in 1° increments from −5° to +16° and −10° to +1° in the X and Y, respectively. For each current measurement, the angular position was held for a period of 2 s, during which 20–24 current measurements were recorded and averaged before moving to the next measurement position. Figure 7(b) plots the 1D beam current profile as a function of X-angle. The data plotted in (b) was extracted from the red-outlined region shown in the 2D heatmap (a), spanning −4° to −8° in Y. Each of the datapoints were calculated for each X-angle by averaging the current along the Y-angles. The solid datapoints show the averaged measurements, and the errorbars represent ±1 standard deviation. The X-angle positions in (b) have all been shifted by 4° to align the beam center with 0° for interpretation and analysis.

The extracted 1D profile in figure 7(b) provides a quantitative measure of beam divergence in the angular X-direction. The approximately Gaussian shape of the distribution suggests that the bulk of the transmitted current is confined within a limited angular spread, which is consistent with expectations of space-charge-limited electrosprays in the cone-jet regime [42, 43]. Using the 1D profile, the beam divergence half-angle was calculated to be approx. 4.3° and 8.8° at 80% and 99% confidence intervals, which are consistent with previously reported single-emitter divergence measurements [44, 45].

A slight left-right asymmetry is observed in the angular current distribution of figure 7(b), suggesting a minor non-uniformity in the beam structure along the pitch direction. This asymmetry may arise from several factors, including small alignment offsets between the emitter and extractor. Additionally, mechanical backlash or positioning uncertainty in the 2D scanning system may contribute to the observed asymmetry and is difficult to fully decouple from intrinsic beam structure. These effects can introduce a small angular bias in the measured current distribution but do not significantly affect the overall beam divergence trends reported.

3.4. Performance metrics

Performance metrics for the TPP-printed emitters were computed using the results of I–V (figure 5) and TOF (figure 6) measurements. Specific impulse I_{sp} describes the efficiency of thrust generation, and is defined by the ratio of thrust F to mass flow rate $\dot{m}$:

$$I_{sp} = \frac{1}{g}\frac{F}{\dot{m}} \tag{1}$$

Here, the force and mass flow rate are computed from the TOF data of figure 6 using the integral formulations [36]:

$$F = \frac{2V_{em}I_{em}}{L_{TOF}}\int_0^{\infty} I_{TOF}\mathrm{d}t \tag{2}$$

Table 3. Estimated performance metrics for a single TPP-printed glass emitter.

Voltage (V)	Current (nA)	Thrust (nN)	Thrust/Power (mN/kW)	I_{sp} (s)
2500	500	64 (75/52)	51	3227 (1785/4669)
-2500	400	46 (47/46)	48	2251 (1925/2578)

$$\dot{m} = \frac{4V_{em}I_{em}}{L_{TOF}^2}\int_0^\infty tI_{TOF}\mathrm{d}t \tag{3}$$

where V_{em} is the emission potential, I_{em} is the emission current, and L_{TOF} is the length from the gate to the detector of the TOF system (0.9526 m for these analyses). I_{TOF} is the normalized current signal from the TOF measurements (figure 6). Table 3 summarizes the resulting performance estimates for a single TPP-printed emitter under both operating polarities (± 2500 V) using the emission current and collected current from the *I–V* and TOF diagnostics. The thrust and I_{sp} metrics were calculated using both the on-axis and off-axis TOF spectra from figure 6. The average values are reported in the table, with the on-axis and off-axis calculated values in the parenthesis (on-axis/off-axis). Here, average I_{sp} values fall in the range of 2200–3300 s, placing them within the upper end of the range typically reported for conventional electrospray devices (approx. 1000–3500 s, depending on the propellant and the operating conditions) [13, 36, 46–48]. However, significant variability is observed between on-axis and off-axis estimates, particularly in positive mode, where the off-axis and on-axis values reach 4669 s and 1785 s, respectively. This spread is attributed to the increased fraction of droplets and heavier species detected in the on-axis TOF spectra (figure 6(a)), which disproportionately lowers the calculated I_{sp}. In addition to the comparably high I_{sp} values, the estimated average single-emitter thrusts of 46 nN (negative) and 64 nN (positive) fall well within the range of typical values reported for conventional electrospray thrusters (per-emitter thrusts of approx. 10–100 nN) [13, 36, 48]. Overall, these results demonstrate that the TPP-printed emitters can achieve performance comparable to traditional ionic liquid electrospray emitters, while offering additional flexibility in emitter geometry and internal structure that is not readily accessible with traditional emitter fabrication techniques.

4. Conclusion

This work demonstrates the capabilities of TPP printing for fabrication of fused-silica electrospray emitters. The unique features of TPP printing enable emitter designs with highly complex architectures and embedded microporous networks to promote passive propellant transport throughout the emitter body. Optical profilometry and SEM characterization confirmed that emitters could be fabricated with tight tolerances to their target CAD geometries, with uniform thermal shrinkage preserving overall emitter geometry. Emission testing showed highly linear *I–V* behavior, with moderate onset voltages (2.4–2.6 kV) and consistent operation across consecutive runs. TOF measurements revealed well-defined charge-state distributions characteristic of EMI-BF_4 electrosprays in the quasi-pure ion regime, with clear differences between positive and negative polarity operation. Performance analysis yielded thrusts of 40–70 nN with specific impulse values exceeding 3000 s, comparable to conventionally-fabricated electrospray devices. However, the primary contribution of this work is not performance enhancement, but rather the demonstration of TPP emitter fabrication that enables deterministic control over both external emitter geometry and internal microstructure.

While this work focuses on single-emitter devices, practical electrospray propulsion systems typically require large emitter arrays to achieve mission-relevant thrust levels. The fabrication approach presented here is well-suited for emitter arrays, as TPP printing enables precise and repeatable placement of emitters with controlled spacing and geometry. However, several considerations arise when scaling to arrays. In particular, total print time scales approximately linearly with emitter count due to the serial nature of TPP printing, which may limit throughput for large-scale fabrication, requiring process optimizations to reduce print time. Additionally, inter-emitter spacing and alignment to the extraction electrode(s) become increasingly critical, as small positional offsets can lead to non-uniform emission and beam interference. TPP printing provides highly accurate placement of emitters to enable precise and consistent inter-emitter spacing, and allow accurate alignment with the extraction electrode(s). The ability to integrate complex porous networks directly into the emitter body offers new opportunities for

scalable array architectures, improved propellant transport, and tailored plume characteristics. Future work will focus on scaling this approach to multi-emitter arrays, refining TPMS morphology to improve fluid transport and wetting characteristics, and optimizing emission stability and efficiency for sustained, repeatable operation.

Acknowledgments

This work was performed in part at the Cornell NanoScale Facility (CNF), a member of the National Nanotechnology Coordinated Infrastructure (NNCI), which is supported by the National Science Foundation (Grant NNCI-2025233). This work made use of the Cornell Center for Materials Research (CCMR) shared instrumentation facility.

Data availability statement

All data that support the findings of this study are included within the article (and any supplementary files).

Funding

This work was financially supported by the DARPA TALOS Grant (Contract Number HR00112490389).

Author contributions

Bryce Kingsley 0009-0003-8402-3292
Formal analysis (lead), Investigation (lead), Methodology (lead), Resources (lead), Writing – original draft (lead), Writing – review & editing (lead)

Nikolaos Chalmpes 0000-0003-2744-5934
Resources (supporting), Writing – original draft (supporting)

Stefan Bell 0000-0002-2881-5944
Investigation (supporting)

Zach Ulibarri 0000-0002-1094-9266
Investigation (supporting)

Emmanuel Giannelis 0000-0001-6158-3738
Conceptualization (supporting), Project administration (supporting), Supervision (supporting)

Sadaf Sobhani 0000-0002-7088-7773
Conceptualization (equal), Funding acquisition (equal), Project administration (equal), Supervision (equal), Writing – review & editing (supporting)

Elaine Petro 0000-0002-4933-5405
Conceptualization (equal), Funding acquisition (equal), Project administration (equal), Supervision (equal), Writing – review & editing (supporting)

References

[1] Courtney D G, Li H and Lozano P C 2013 Electrochemical micromachining on porous nickel for arrays of electrospray ion emitters *J. Microelectromech. Syst.* **22** 471–82
[2] Legge R S and Lozano P C 2011 Electrospray propulsion based on emitters microfabricated in porous metals *J. Propuls. Power* **27** 485–95
[3] Xue S, Duan L and Kang Q 2021 Fabrication of externally wetted emitter for ionic liquid electrospray thruster by low-speed wire cutting combined with electrochemical etching *AIP Adv.* **11** 115023
[4] Seo W G, Kuk J W, Kim H, Kang D and Huh J 2023 Micro/nano scale emission tip fabrication for field emission electric propulsion *2023 IEEE 22nd Int. Conf. on Micro and Nanotechnology for Power Generation and Energy Conversion Applications (PowerMEMS)* pp 252–5
[5] Velasquez-Garcia L, Akinwande A and Martinez-Sanchez M 2006 A micro-fabricated linear array of electrospray emitters for thruster applications *J. Microelectromech. Syst.* **15** 1260–71

[6] Velasquez-Garcia L, Akinwande A and Martinez-Sanchez M 2006 A planar array of micro-fabricated electrospray emitters for thruster applications *J. Microelectromech. Syst.* **15** 1272–80
[7] Gassend B, Velasquez-Garcia L, Akinwande A and Martinez-Sanchez M 2008 Fabrication of a fully integrated electrospray array with applications to space propulsion *2008 IEEE 21st Int. Conf. on Micro Electro Mechanical Systems* pp 976–9
[8] Inoue N, Nagao M, Murakami K, Khumpuang S, Hara S and Takao Y 2019 Fabrication of a high-density emitter array for electrospray thrusters using field emitter array process *Jpn. J. Appl. Phys.* **58** SEEG04
[9] Suzuki K, Nagao M, Liu Y, Murakami K, Khumpuang S, Hara S and Takao Y 2021 Fabrication of nano-capillary emitter arrays for ionic liquid electrospray thrusters *Jpn. J. Appl. Phys.* **60** SCCF07
[10] Dandavino S, Ataman C, Ryan C N, Chakraborty S, Courtney D, Stark J P W and Shea H 2014 Microfabricated electrospray emitter arrays with integrated extractor and accelerator electrodes for the propulsion of small spacecraft *J. Micromech. Microeng.* **24** 075011
[11] Cisquella-Serra A, Galobardes-Esteban M and Gamero-Castaño M 2022 Scalable microfabrication of multi-emitter arrays in silicon for a compact microfluidic electrospray propulsion system *ACS Appl. Mater. Interfaces* **14** 43527–37
[12] Li L, Yang W, Zhao X and Deng W 2020 Multiplexed electrospray emitters fabricated by rapid laser micromachining *J. Aerosol. Sci.* **150** 105616
[13] Natisin M R and Zamora H L 2019 Performance of a fully conventionally machined liquid-ion electrospray thruster operated in pir *2019 36th Int. Electric Propulsion Conf.*
[14] Kachkine A and Velásquez-García L F 2024 High-performance, low-cost, additively manufactured electrospray ion sources for mass spectrometry *J. Am. Soc. Mass Spectrom.* **35** 862–70
[15] Chamieh S, Petro E and Sobhani S 2023 Additive manufacturing and characterization of porous ceramic electrospray emitters *AIAA SCITECH 2023 Forum* (*National Harbor, MD& Online*) (American Institute of Aeronautics and Astronautics)
[16] Chamieh S, D'Cruz L S, Petro E and Sobhani S 2024 Characterization and testing of additively manufactured porous ceramic electrospray emitters *AIAA SCITECH 2024 Forum* (*Orlando, FL*) (American Institute of Aeronautics and Astronautics)
[17] Kunze F L, Henning T and Klar P J 2024 3D micro printed capillary electrospray thruster with a fully modular integrated extraction electrode *J. Electr. Propuls.* **3** 3
[18] Kim H and Velásquez-García L F 2025 High-impulse, modular, 3D-printed cubesat electrospray thrusters throttleable via pressure and voltage control *Adv. Sci.* **12** 2413706
[19] Doualle T, André J-C and Gallais L 2021 3D printing of silica glass through a multiphoton polymerization process *Opt. Lett.* **46** 364
[20] Rad Z F, Prewett P D and Davies G J 2021 High-resolution two-photon polymerization: the most versatile technique for the fabrication of microneedle arrays *Microsyst. Nanoeng.* **7** 71
[21] Bunea A-I, Iniesta N D C, Droumpali A, Wetzel A E, Engay E and Taboryski R 2021 Micro 3D printing by two-photon polymerization: configurations and parameters for the nanoscribe system *Micro* **1** 164–80
[22] Maruo S, Nakamura O and Kawata S 1997 Three-dimensional microfabrication with two-photon-absorbed photopolymerization *Opt. Lett.* **22** 132
[23] Amruth C, Singh A K, Sharma A, Corzo D and Baran D 2024 Micro-3D printed conductive polymer composite via two-photon polymerization for sensing applications *Adv. Mater. Technol.* **9** 2400290
[24] Im J *et al* 2023 Strategies for integrating metal nanoparticles with two-photon polymerization process: toward high resolution functional additive manufacturing *Adv. Funct. Mater.* **33** 2211920
[25] Kilic N I, Saladino G M, Johansson S, Shen R, McDorman C, Toprak M S and Johansson S 2023 Two-photon polymerization printing with high metal nanoparticle loading *ACS Appl. Mater. Interfaces* **15** 49794–804
[26] Prediger R, Sriyotha N, Schell K G, Kluck S, Hambitzer L and Kotz-Helmer F 2024 Two-photon polymerization of nanocomposites for additive manufacturing of transparent magnesium aluminate spinel ceramics *Adv. Sci.* **11** 2307175
[27] Arriaga-Dávila J *et al* 2025 From single to multi-material 3D printing of glass-ceramics for micro-optics *Small Methods* **9** 2401809
[28] Bauer J, Crook C and Baldacchini T 2023 A sinterless, low-temperature route to 3D print nanoscale optical-grade glass *Science* **380** 960–6
[29] Kunze F L, Henning T and Klar P J 2021 Taking internally wetted capillary electrospray emitters to the sub-ten-micrometer scale with 3D microlithography *AIP Adv.* **11** 105315
[30] Xing L, Liu D, Yu H, Ding H, Sun J, Wang G, Deng Y, Chang W and Xie Z 2025 Two-photon direct laser writing of capillary-coupled nanosprayer arrays for ESI-MS *Anal. Chem.* **97** 3713–9
[31] Takagi K, Tsukizaki R and Takao Y 2025 Variability trend and geometry effect of a single emitter on ion emission in passively fed porous ionic liquid electrospray thrusters *J. Appl. Phys.* **58** 445504
[32] Krejci D, Mier-Hicks F, Fucetola C and Lozano P yr2015 Design and characterization of a scalable ion electrospray propulsion system *34th Int. Electric Propulsion Conf.*
[33] Kerber T, Taylor N, Lemmer K, Meza A, Antypas R, Stahl V and Eckhardt D 2025 Stochastic emission in passively fed single-emitter porous-media ionic liquid ion sources *J. Propuls. Power* **41** 190–9
[34] Wright P L and Wirz R E 2024 Transient flow in porous electrosprays *Transp. Porous Media* **151** 2277–99
[35] Jia-Richards O 2022 Quantification of ionic-liquid ion source beam composition from time-of-flight data *J. Appl. Phys.* **132** 074501
[36] Petro E, Bruno A, Lozano P, Perna L E and Freeman D 2020 Characterization of the TILE electrospray emitters *AIAA Propulsion and Energy 2020 Forum* (American Institute of Aeronautics and Astronautics)
[37] Hofheins G C, Ulibarri Z and Petro E M 2025 Electrospray propulsion time-of-flight secondary ion mass spectrometry diagnostic *Rev. Sci. Instrum.* **96** 063306
[38] Caballero-Pérez M and Gamero-Castaño M 2026 Physics of the droplet-to-ion transition in electrosprays of highly conducting liquids (https://doi.org/10.48550/arXiv.2604.04242)
[39] Ulibarri Z and Petro E 2025 True two-dimensional studies of vacuum electrospray ionization plumes *2025 39th Int. Electric Propulsion Conf.*
[40] Ulibarri Z, Hofheins G, Gessman S and Petro E 2026 On the two-dimensional structure and asymmetries of ionic liquid electrospray plumes (https://doi.org/10.48550/arXiv.2605.24129)
[41] Ulibarri Z and Petro E 2025 Direct two-dimensional goniometric steering of vacuum electrospray ion beams for angular time-of-flight studies *Rev. Sci. Instrum.* **96** 043301
[42] Taziny A, Chan W H R and Boyd I D 2025 Hybrid modeling of ionic emission and plume dynamics in electrospray thrusters *J. Electr. Propuls.* **4** 32

[43] Petro E M, Gallud X, Hampl S K, Schroeder M, Geiger C and Lozano P C 2022 Multiscale modeling of electrospray ion emission *J. Appl. Phys.* **131** 193301
[44] Schroeder M, Cidoncha X G, Bruno A, Jia-Richards O and Lozano P 2023 Angular properties of ionic liquid electrospray emitters *AIAA SCITECH 2023 Forum*
[45] Gamero-Castaño M 2008 The structure of electrospray beams in vacuum *J. Fluid Mech.* **604** 339–68
[46] Caballero-Pérez M, Galobardes-Esteban M, and Gamero-Castaño M 2026 High specific impulse electrospray propulsion with small capillary emitters *J. Propuls. Power* **42** 227–39
[47] Huang C, Li J and Li M 2023 Performance measurement and evaluation of an ionic liquid electrospray thruster *Chin. J. Aeronaut.* **36** 1–15
[48] Whittaker C, Arestie S, Marrese-Reading C and Jorns B 2025 Characterization of a 10 W class electrospray array thruster *J. Electr. Propuls.* **4** 20